

# Mesoscopic Spin Coherence in a Disordered Dark Electron Spin Ensemble

Taewoong Yoon,<sup>1,2</sup> Sangwon Oh,<sup>3</sup> Junghyun Lee,<sup>4,\*</sup> and Hyunyong Choi<sup>1,2,†</sup>

<sup>1</sup>*Department of Physics and Astronomy, Seoul National University, Seoul 08826, Korea*

<sup>2</sup>*Institute of Applied Physics, Seoul National University, Seoul 08826, Korea*

<sup>3</sup>*Department of Physics and Department of Energy Systems Research, Ajou University, Suwon 16499, Korea*

<sup>4</sup>*Center for Quantum Technology, Korea Institute of Science and Technology, Seoul 02792, Korea*

(Dated: February 20, 2026)

Harnessing dipolar spin environments as controllable quantum resources is a central challenge in solid-state quantum technologies. Here, we report the observation of a coherent mesoscopic spin state in a disordered ensemble of substitutional nitrogen (P1) centers in diamond. An iterative Hartmann-Hahn protocol transfers polarization from dense nitrogen-vacancy (NV) centers to a P1 ensemble, yielding a 740-fold enhancement over room-temperature thermal equilibrium as revealed by differential readout. The resulting mesoscopic P1 spin ensemble exhibits collective Rabi oscillations and long-lived spin-lock and Hahn-echo coherences. We identify a crossover in the saturation polarization arising from the competition between coherent driving and local disorder, providing a quantitative measure of the system's intrinsic disorder. These results establish a foundation for utilizing dark electron spin ensembles as robust resources for quantum sensing and quantum many-body simulation.

Solid-state spin systems have emerged as a compelling platform for quantum information science, ranging from nanoscale magnetometry to probing many-body dynamics [1–5]. Although surrounding spin environments are typically regarded as a primary source of decoherence [6, 7], their large Hilbert space can be exploited as a powerful quantum resource. This potential motivates the use of proximal nuclear and electronic spins as long-lived quantum memories and registers [8–11], the realization of environment- and logic-assisted sensing protocols in which ancillary spins enhance sensitivity [12–14], and the exploitation of dense spin ensembles as analog quantum simulators of emergent phenomena [15–17].

Among spin environments, substitutional nitrogen (P1) centers constitute the dominant paramagnetic defects in diamond, typically outnumbering nitrogen-vacancy (NV) centers owing to the limited conversion efficiency during synthesis [18–20]. In contrast to well-established NV spin qubits with robust optical initialization and readout [21], the more abundant P1 centers form an optically dark electronic spin bath that limits NV coherence [6, 7]. Exploiting these dark spins as a quantum resource requires polarization transfer from NV centers, commonly achieved via resonant spin flip-flop interactions at specific external magnetic fields [16, 22, 23]. Alternatively, spin-locking (SL) under the Hartmann-Hahn (HH) condition offers a more versatile pathway for polarization exchange in the rotating frame [24–26]. This method enables control over both the coupling strength and the effective disorder [27, 28]. However, previous approaches often rely on isolated NV centers to polarize local environments [26, 29], where polarization rapidly dissipates via spin diffusion into the bulk thermal reservoir [23, 30, 31]. As a result, robust mesoscopic polarization in disordered P1 ensembles has remained unrealized.

In this Letter, we demonstrate the generation and con-

trol of a coherent mesoscopic spin state in a disordered ensemble of dark P1 centers in diamond. To prepare and interrogate this state, we employ an iterative HH protocol combined with a polarization-direction-differential readout scheme. Leveraging a dense NV network, we achieve a 740-fold enhancement of P1 ensemble polarization over the room-temperature thermal limit. The rapid saturation observed within a few transfer cycles indicates that additional relaxation channels during NV initialization play a critical role in the P1 polarization process. We observe collective Rabi oscillations and characterize robust SL relaxation and Hahn-echo coherence times. Moreover, we identify a crossover in the saturation polarization where coherent driving overcomes local disorder to enable efficient polarization exchange. Together, these results demonstrate that disordered spin environments can be transformed into robust quantum resources.

Our experiments are conducted on a hybrid electron spin ensemble embedded in an isotopically purified diamond substrate at room temperature [Fig. 1(a)]. The sample contains high concentrations of P1 centers ( $[P1] \approx 6.3$  ppm) and NV centers ( $[NV] \approx 2.4$  ppm) [32], corresponding to  $\sim 10^5$  spins within the probed volume. Each P1 center hosts an optically dark electron spin ( $S = 1/2$ ) subject to strong hyperfine coupling to its host  $^{14}\text{N}$  nucleus ( $I = 1$ ) and Jahn-Teller (JT) distortion [10, 33]. We apply a bias magnetic field of  $B_z = 446$  G along the NV symmetry axis to lift the spin-state degeneracy, allowing us to treat the  $\{|0\rangle, |-1\rangle\}$  subspace of the spin-1 NV ground state as an effective spin-1/2 system.

Due to the substantial Zeeman energy mismatch between the two electron spin species, the dipolar Hamiltonian is reduced to a secular Ising interaction,  $H_{\text{int}} = \sum_{i < j} J_{ij} S_i^z S_j^z$ , where  $S_i$  denotes the spin operator of the  $i$ -th spin and  $J_{ij}$  is the dipolar coupling strength. To bridge the energy mismatch, we employ SL, where reso-

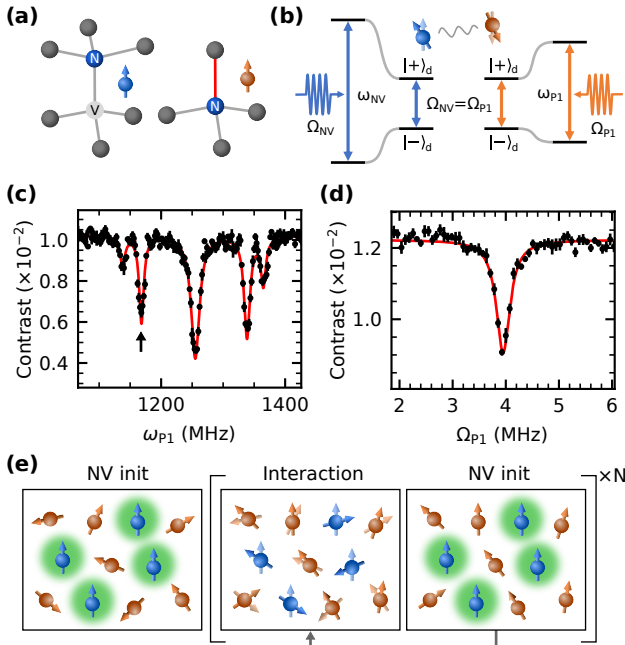


FIG. 1. NV-P1 hybrid electron spin system and polarization transfer protocol. (a) Atomic structures of the NV (left) and P1 (right) centers. Spheres represent carbon atoms (gray), nitrogen atoms (blue), and vacancies (light gray). The P1 JT axis is highlighted in red. Blue and orange arrows denote NV and P1 electron spins, respectively. (b) HH condition. Two spin species with distinct resonance frequencies  $\omega_{NV}$  and  $\omega_{P1}$  are resonantly driven at Rabi frequencies  $\Omega_{NV}$  and  $\Omega_{P1}$ , respectively. In the dressed-state basis  $\{|+\rangle_d, |-\rangle_d\}$ , the energy splittings are matched when  $\Omega_{NV} = \Omega_{P1}$ . (c) P1 electron spin resonance spectrum measured via DEER. The hyperfine interaction and JT distortion result in five visible spectral subgroups with population fractions of  $\{1, 3, 4, 3, 1\}/12$ . We address a P1 subgroup with a population fraction of  $3/12$  (indicated by an arrow) for polarization transfer measurements. The solid red line represents a multi-Lorentzian fit. (d) Measurement of the HH resonance condition. NV SL contrast is plotted as a function of the P1 Rabi frequency  $\Omega_{P1}$ , with  $\Omega_{NV} = 3.95$  MHz. The solid line represents a Lorentzian fit. (e) Iterative polarization transfer protocol. The sequence comprises optical NV initialization followed by interaction with the P1 ensemble under the HH condition. This cycle is repeated to accumulate polarization in the P1 ensemble. Error bars represent s.e.m.

nant driving defines a dressed-state energy splitting equal to the Rabi frequency  $\Omega$  [Fig. 1(b)]. Under driving along the  $x$ -axis, which defines the effective quantization axis in the rotating frame, the longitudinal Ising coupling is converted into spin flip-flop interactions, as the original  $S^z$  operators become transverse in the dressed-state basis. When the Rabi frequencies satisfy the HH condition ( $\Omega_{NV} = \Omega_{P1} = \Omega$ ), the NV-P1 system undergoes resonant spin exchange [25, 26]. In the strong driving limit ( $\Omega \gg W$ ), the effective disorder in the dressed frame is reduced to  $W_{\text{eff}} \approx W^2/(2\Omega)$ , where  $W$  denotes the char-

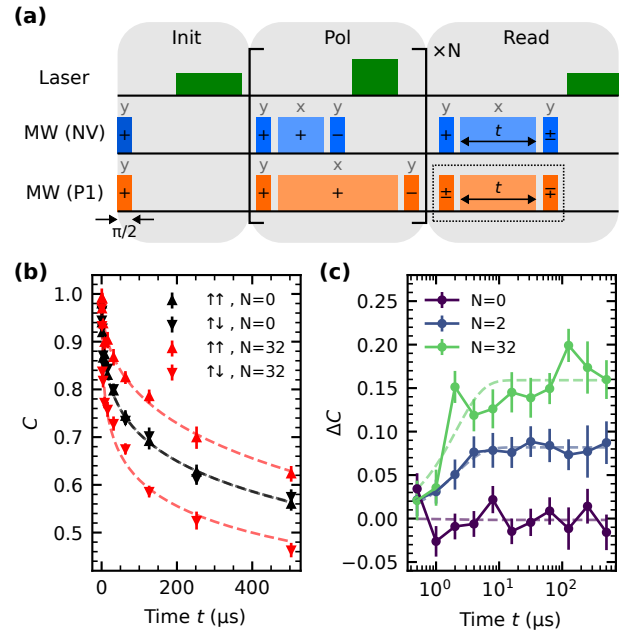


FIG. 2. Polarization transfer pulse sequences and polarization dynamics. (a) Detailed pulse sequences. Light (dark) colors represent microwave pulses along the  $x$  ( $y$ ) axis. The polarization transfer stage involves 5  $\mu$ s of DSL under the HH condition and 5  $\mu$ s of laser illumination. In the subsequent readout stage, the signal is obtained by sweeping the duration  $t$  of the second DSL sequence. For the NV (blue), the final  $\pi/2$  pulse employs phase cycling ( $\pm$ ) for common-mode noise rejection. For the P1 (orange), the pulses in the dotted box prepare the P1 bath polarization parallel ( $\uparrow\uparrow$ ) or antiparallel ( $\uparrow\downarrow$ ) to the NV. In the absence of these pulses, the sequence measures the reference bare NV SL. (b) Normalized SL signal  $C$  for parallel and antiparallel configurations ( $\Omega = 6.40$  MHz). Data are shown for the thermal state ( $N = 0$ , black) and after iterative transfer ( $N = 32$ , red). Dashed lines indicate stretched exponential fits. (c) Signal difference  $\Delta C$  versus SL duration  $t$  for varying cycle numbers  $N$ . Dashed lines are exponential fits. Error bars represent s.e.m.

acteristic disorder scale [27, 34].

We characterize the energy spectrum of the dark P1 ensemble using double electron-electron resonance (DEER), and the HH resonance using double spin-locking (DSL) [25, 33]. The DEER spectrum exhibits five distinct subgroups with population fractions of  $\{1, 3, 4, 3, 1\}/12$ , arising from the three  $^{14}\text{N}$  nuclear spin states and the four JT distortion axes [Fig. 1(c)]. For the subsequent experiments, we focus on the subgroup with a  $3/12$  population fraction. The HH resonance is experimentally verified by a pronounced Lorentzian dip in the DSL contrast when the Rabi frequencies are matched [Fig. 1(d)]. Based on these results, we implement an iterative protocol comprising repetitive cycles of optical NV initialization and HH interaction to accumulate polarization in the P1 bath [Fig. 1(e)]. Here, NV centers act as both optically active polarization sources and sensors to

read out the collective state of the P1 ensemble.

We probe the accumulation of P1 polarization using the pulse sequence depicted in Fig. 2(a). To eliminate readout artifacts and isolate the signal originating from the probed NV centers, we employ a common-mode rejection scheme by subtracting two signals acquired with  $\pi/2$  pulses of opposite phase [27]. Additionally, we normalize the DSL signal to the bare NV SL decay measured in the absence of P1 driving. This allows us to extract the P1 polarization dynamics mediated by dipolar interactions, independent of intrinsic NV relaxation.

Fig. 2(b) shows the normalized SL signals  $C$  obtained after  $N = 32$  transfer cycles for two different polarization configurations. We observe a prominent asymmetry between parallel ( $\uparrow_{\text{NV}}\uparrow_{\text{P1}}$ ) and antiparallel ( $\uparrow_{\text{NV}}\downarrow_{\text{P1}}$ ) P1 bath configurations relative to the NV spin. The parallel configuration suppresses energy-conserving flip-flops, extending the DSL lifetime, whereas the antiparallel configuration accelerates the decay. Thus, the difference signal  $\Delta C = C_{\uparrow\uparrow} - C_{\uparrow\downarrow}$  serves as a direct measure of the net P1 polarization.

The temporal evolution of  $\Delta C$  [Fig. 2(c)] reveals the polarization exchange dynamics during the readout DSL time  $t$ . The signals rise and level off, indicating that the NV and P1 ensembles reach a transient quasi-equilibrium. The dynamics are well described by an exponential function  $\Delta C(t) = A(1 - e^{-t/\tau_{\text{eq}}})$  with a characteristic time  $\tau_{\text{eq}} = 2.2 \pm 0.6 \mu\text{s}$ . This timescale is over two orders of magnitude shorter than the NV SL relaxation time  $T_{1\rho}^{\text{NV}} \approx 1.3 \text{ ms}$ . The distinct separation of timescales confirms that the observed equilibration is driven by resonant NV-P1 spin exchange, rather than by intrinsic NV relaxation channels.

We estimate the absolute polarization of the P1 bath by invoking conservation of total angular momentum in the rotating frame. From the concentration ratio  $n_{\text{P1}}/n_{\text{NV}} \approx 2.6$  and the quasi-equilibrium signal amplitude  $A$ , we determine the P1 polarization as  $P^{\text{P1}} = P_0^{\text{NV}}(A/2)(1 + n_{\text{NV}}/n_{\text{P1}})$  [32]. Assuming an initial NV polarization of  $P_0^{\text{NV}} \approx 75\%$  [35] and the saturation amplitude  $A_\infty \approx 0.143$  in the strong-driving limit [cf. Fig. 4(b)], we estimate a P1 polarization of  $P^{\text{P1}} \approx 7.4\%$ . This corresponds to a polarization enhancement of approximately 740-fold compared to the thermal equilibrium polarization of  $\sim 0.010\%$  at room temperature under the bias field. Converting this polarization into an effective spin temperature via  $T_{\text{spin}} = \hbar\gamma_e B/(2k_B \tanh^{-1} P^{\text{P1}})$  yields  $T_{\text{spin}} \approx 405 \text{ mK}$ . These results show that our protocol effectively prepares a low-entropy mesoscopic spin state from a thermal mixed state.

To verify the coherent nature of the polarized bath, we perform collective manipulation. The readout stage likewise employs the HH condition to coherently map the P1 ensemble spin polarization back onto the NV centers for optical detection. By inserting a control pulse sequence

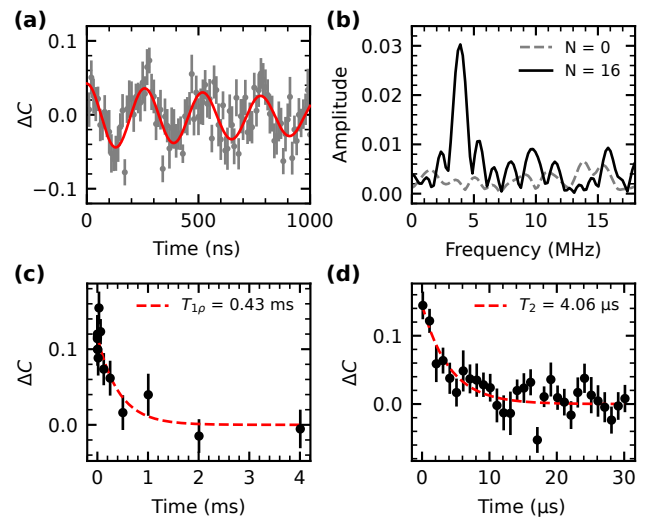


FIG. 3. Coherent control and relaxation dynamics of the polarized P1 ensemble. (a) Collective Rabi oscillations of the P1 bath measured after  $N = 16$  transfer cycles. The solid red line represents a fit to a damped cosine function. (b) FFT spectra of the Rabi signal. A distinct frequency component appears for the polarized state ( $N = 16$ , black), whereas no signature is visible for the thermal state ( $N = 0$ , gray). (c) Rotating-frame spin relaxation time ( $T_{1\rho}$ ) measured via SL. (d) Measured Hahn-echo spin dephasing time ( $T_2$ ). Dashed red lines in (c) and (d) are fits to exponential decays. Error bars represent s.e.m.

between the polarization and readout blocks, we observe clear Rabi oscillations of the P1 ensemble [Fig. 3(a)]. These measurements are performed at  $N = 16$  cycles, well into the saturation regime [cf. Fig. 4(a)], ensuring that the P1 bath has reached its steady-state polarization. The fast Fourier transform (FFT) of the signal shows a distinct frequency component associated with the driven P1 spins, which is absent in the unpolarized thermal state ( $N = 0$ ) [Fig. 3(b)].

It is essential to distinguish this observation from conventional DEER oscillations measured in a thermal bath [33]. In a standard DEER measurement, the oscillating signal originates from modulation of NV decoherence by fluctuating local fields of an unpolarized P1 bath. Such measurements probe correlations, but do not indicate collective coherence of the bath. In contrast, our measurement directly probes the population dynamics of the P1 ensemble. The absence of oscillations at  $N = 0$  and their emergence at  $N = 16$  confirm that we coherently manipulate a net mesoscopic polarization.

We then characterize the relaxation dynamics of the spin-initialized P1 ensemble. The rotating-frame relaxation time, which sets the effective lifetime for SL operations, is measured to be  $T_{1\rho}^{\text{P1}} = 0.43 \pm 0.16 \text{ ms}$  [Fig. 3(c)]. Notably, the measured  $T_{1\rho}^{\text{P1}}$  is comparable to the independently measured  $T_1^{\text{P1}} \approx 0.67 \text{ ms}$ , which indicates that

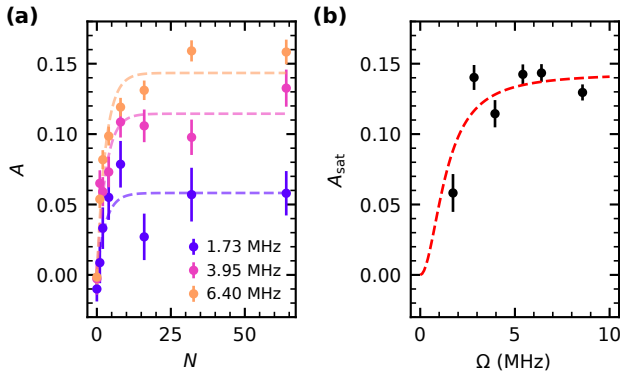


FIG. 4. Competition between coherent driving and disorder. (a) Quasi-equilibrium amplitude  $A$  versus cycle number  $N$  for various P1 Rabi frequencies  $\Omega$ . The signal saturates as the polarization transfer rate balances with dissipation. Dashed lines are exponential fits. (b) Dependence of the saturation amplitude  $A_{\text{sat}}$  on  $\Omega$ . The signal enhancement at higher Rabi frequencies indicates that strong driving suppresses the local disorder, thereby facilitating spin transport across the ensemble. The red dashed line is a fit to the phenomenological model described in the text. Error bars indicate fitting uncertainties.

rotating-frame relaxation is governed by the same intrinsic processes that limit  $T_1$ , rather than by rapid polarization diffusion into the surrounding unpolarized bulk. Furthermore, the Hahn-echo dephasing time is measured to be  $T_2^{\text{P}1} = 4.06 \pm 0.78 \mu\text{s}$  [Fig. 3(d)]. The ratio of this value to the NV dephasing time ( $T_2^{\text{NV}} = 10.7 \pm 1.0 \mu\text{s}$ ),  $T_2^{\text{NV}}/T_2^{\text{P}1} \approx 2.6$ , is consistent with the defect density ratio. This correspondence supports a picture in which Hahn-echo dephasing in both ensembles is dominated by intragroup dipolar flip-flop interactions, while intergroup Ising couplings are refocused by the echo [6].

To investigate the limits of the iterative polarization protocol, we monitor the buildup of the polarization as a function of the cycle number  $N$  [Fig. 4(a)]. The saturation indicates that the local P1 bath reaches a steady state, in which polarization injection from the NV centers is counterbalanced by dissipation. The buildup dynamics are well described by  $A(N) = A_{\text{sat}}(1 - e^{-N/N_{\text{sat}}})$ , with characteristic cycle number  $N_{\text{sat}} \approx 3$ . Given a period of  $10 \mu\text{s}$  per cycle, this corresponds to a saturation timescale of  $\tau_{\text{sat}} \approx 30 \mu\text{s}$ , an order of magnitude shorter than the  $T_{1\rho}^{\text{P}1}$  measured in the dark. To understand this rapid saturation, we employ a semiclassical master equation on a disordered spin network [32]. Fitting the observed saturation cycles yields an effective P1 relaxation time of  $T_{1\rho, \text{laser}}^{\text{P}1} \approx 32 \mu\text{s}$  during laser illumination. We attribute this enhanced relaxation to photo-ionization of P1 centers by the  $532 \text{ nm}$  pulse and charge-state dynamics of nearby NV centers [36–38]. While capturing the qualitative saturation behavior, the model overestimates the absolute polarization by a factor of 2–3, suggesting additional

dissipation beyond our pairwise description.

Fig. 4(b) shows the dependence of the saturation amplitude  $A_{\text{sat}}$  on the Rabi frequency  $\Omega$ , reflecting the competition between coherent driving strength and intrinsic disorder. In the hybrid electron spin network, the random spatial distribution of P1 centers creates an inhomogeneous energy landscape with characteristic disorder scale  $W$ . In the weak driving regime ( $\Omega < W$ ), energy mismatches between neighboring spins suppress resonant flip-flop interactions, whereas in the strong driving regime ( $\Omega > W$ ), these mismatches are overcome. This crossover is captured by  $A_{\text{sat}}(\Omega) = A_{\infty}\Omega^2/(\Omega^2 + W^2)$ , and fitting yields  $W = 1.36 \pm 0.19 \text{ MHz}$ , which determines the effective disorder scale of the system.

The spatial extent of the steady-state polarization is governed by spin diffusion within the network. Numerical simulations yield a spin diffusion coefficient  $D \approx 0.22 \text{ nm}^2/\mu\text{s}$  from the mean-squared displacement of the polarization distribution [32], corresponding to a diffusion length  $L_D = \sqrt{6D\tau_{\text{sat}}} \approx 6.2 \text{ nm}$  over the saturation timescale. Although the mean nearest-neighbor distance  $d_{\text{NN}} \approx 11.7 \text{ nm}$  of the addressed NV subgroup ( $[\text{NV}] \approx 0.6 \text{ ppm}$ ) exceeds  $L_D$ , Poisson statistics indicate that approximately 57% of NV centers have at least one neighbor within the overlap distance  $2L_D$ . The resulting polarization clusters, where overlapping diffusion fronts reduce the local polarization gradient, suppress outward spin diffusion and stabilize the steady-state polarization lifetime.

In conclusion, we demonstrate that an iterative Hartmann-Hahn protocol with a dense NV network generates a coherent mesoscopic spin state in a disordered P1 ensemble, achieving a 740-fold polarization enhancement over room-temperature thermal equilibrium. The emergence of collective Rabi oscillations verifies the coherent nature of the polarized state, while subsequent characterization reveals long-lived spin-lock and Hahn-echo lifetimes. Rabi-frequency-dependent saturation exposes a competition between coherent driving and local disorder, and suggests additional dissipation pathways beyond pairwise interactions. The formation of local polarization clusters suppresses outward spin diffusion, extending the polarization lifetime. These results establish dark electron spin ensembles as controllable quantum resources for sensing and simulation.

Further optimization of the polarization process relies on a deeper understanding and control of the underlying dissipation mechanisms, particularly the charge dynamics identified during laser illumination. Future efforts in sample synthesis will focus on balancing the NV-to-P1 ratio to optimize the trade-off between polarization transfer efficiency and the total volume of the available quantum resource. Beyond materials engineering, the implementation of advanced control techniques such as Hamiltonian engineering [39, 40] and algorithmic cooling [41, 42] offers a pathway to further reduce the effective spin tempera-

ture, by suppressing unwanted depolarization and more efficiently extracting entropy from the spin ensemble.

The ability to prepare and manipulate these mesoscopic states opens broad avenues for quantum sensing and simulation. In sensing, highly polarized P1 ensembles can serve as environment-assisted sensors [43, 44] or as polarization sources for nuclear spins [45], facilitating the generation of metrological states with enhanced sensitivity [46, 47]. As an analog quantum simulator, this platform provides a controllable spin ensemble with tunable dissipation to investigate non-equilibrium quantum thermodynamics. These capabilities further enable the exploration of complex many-body phenomena in disordered dipolar spin networks [48, 49], bridging the gap between controlled few-body quantum systems and macroscopic spin ensembles.

T.Y. and H.C. acknowledge support from the National Research Foundation of Korea (NRF) through the government of Korea (Grant No. 2021R1A2C3005905, RS-2024-00466612, RS-2024-00413957, RS-2023-00258359, RS-2024-00487645) and the Institute for Basic Science (IBS) in Korea (Grant No. IBS-R034-D1). J.L. acknowledges support from the NRF of Korea (Grant No. RS-2025-02219034, RS-2025-25454922, RS-2024-00442710) and the KIST institutional program (Grant No. 2E33541).

D. J. Twitchen, and T. H. Taminiau, A Ten-Qubit Solid-State Spin Register with Quantum Memory up to One Minute, *Physical Review X* **9**, 031045 (2019).

- [9] A. Bourassa, C. P. Anderson, K. C. Miao, M. Onizhuk, H. Ma, A. L. Crook, H. Abe, J. Ul-Hassan, T. Ohshima, N. T. Son, G. Galli, and D. D. Awschalom, Entanglement and control of single nuclear spins in isotopically engineered silicon carbide, *Nature Materials* **19**, 1319 (2020).
- [10] M. J. Degen, S. J. H. Loenen, H. P. Bartling, C. E. Bradley, A. L. Meinsma, M. Markham, D. J. Twitchen, and T. H. Taminiau, Entanglement of dark electron-nuclear spin defects in diamond, *Nature Communications* **12**, 3470 (2021).
- [11] A. Ungar, P. Cappellaro, A. Cooper, and W. K. C. Sun, Control of an Environmental Spin Defect beyond the Coherence Limit of a Central Spin, *PRX Quantum* **5**, 010321 (2024).
- [12] L. Jiang, J. S. Hodges, J. R. Maze, P. Maurer, J. M. Taylor, D. G. Cory, P. R. Hemmer, R. L. Walsworth, A. Yacoby, A. S. Zibrov, and M. D. Lukin, Repetitive Readout of a Single Electronic Spin via Quantum Logic with Nuclear Spin Ancillae, *Science* **326**, 267 (2009).
- [13] N. Arunkumar, K. S. Olsson, J. T. Oon, C. A. Hart, D. B. Bucher, D. R. Glenn, M. D. Lukin, H. Park, D. Ham, and R. L. Walsworth, Quantum Logic Enhanced Sensing in Solid-State Spin Ensembles, *Physical Review Letters* **131**, 100801 (2023).
- [14] A. Cooper, W. K. C. Sun, J.-C. Jaskula, and P. Cappellaro, Environment-assisted Quantum-enhanced Sensing with Electronic Spins in Diamond, *Physical Review Applied* **12**, 044047 (2019).
- [15] D. Pagliero, P. R. Zangara, J. Henshaw, A. Ajoy, R. H. Acosta, J. A. Reimer, A. Pines, and C. A. Meriles, Optically pumped spin polarization as a probe of many-body thermalization, *Science Advances* **6**, eaaz6986 (2020).
- [16] C. Zu, F. Machado, B. Ye, S. Choi, B. Kobrin, T. Mittiga, S. Hsieh, P. Bhattacharyya, M. Markham, D. Twitchen, A. Jarmola, D. Budker, C. R. Laumann, J. E. Moore, and N. Y. Yao, Emergent hydrodynamics in a strongly interacting dipolar spin ensemble, *Nature* **597**, 45 (2021).
- [17] E. J. Davis, B. Ye, F. Machado, S. A. Meynell, W. Wu, T. Mittiga, W. Schenken, M. Joos, B. Kobrin, Y. Lyu, Z. Wang, D. Bluvstein, S. Choi, C. Zu, A. C. B. Jayich, and N. Y. Yao, Probing many-body dynamics in a two-dimensional dipolar spin ensemble, *Nature Physics* **19**, 836 (2023).
- [18] Y. Mindarava, R. Blinder, C. Laube, W. Knolle, B. Abel, C. Jentgens, J. Isoya, J. Scheuer, J. Lang, I. Schwartz, B. Naydenov, and F. Jelezko, Efficient conversion of nitrogen to nitrogen-vacancy centers in diamond particles with high-temperature electron irradiation, *Carbon* **170**, 182 (2020).
- [19] C. Osterkamp, P. Balasubramanian, G. Wolff, T. Teraji, M. Nesladek, and F. Jelezko, Benchmark for Synthesized Diamond Sensors Based on Isotopically Engineered Nitrogen-Vacancy Spin Ensembles for Magnetometry Applications, *Advanced Quantum Technologies* **3**, 2000074 (2020).
- [20] T. Luo, L. Lindner, J. Langer, V. Cimalla, X. Vidal, F. Hahl, C. Schreyvogel, S. Onoda, S. Ishii, T. Ohshima, D. Wang, D. A. Simpson, B. C. Johnson, M. Capelli, R. Blinder, and J. Jeske, Creation of nitrogen-vacancy centers in chemical vapor deposition diamond for sensing applications, *New Journal of Physics* **24**, 033030 (2022).

\* Contact author: jh\_lee@kist.re.kr

† Contact author: hy.choi@snu.ac.kr

- [1] C. L. Degen, F. Reinhard, and P. Cappellaro, Quantum sensing, *Reviews of Modern Physics* **89**, 035002 (2017).
- [2] G. Wolfowicz, F. J. Heremans, C. P. Anderson, S. Kanai, H. Seo, A. Gali, G. Galli, and D. D. Awschalom, Quantum guidelines for solid-state spin defects, *Nature Reviews Materials* **6**, 906 (2021).
- [3] A. Chatterjee, P. Stevenson, S. De Franceschi, A. Morello, N. P. de Leon, and F. Kuemmeth, Semiconductor qubits in practice, *Nature Reviews Physics* **3**, 157 (2021).
- [4] D. D. Awschalom, R. Hanson, J. Wrachtrup, and B. B. Zhou, Quantum technologies with optically interfaced solid-state spins, *Nature Photonics* **12**, 516 (2018).
- [5] J. Rovny, S. Gopalakrishnan, A. C. B. Jayich, P. Maletinsky, E. Demler, and N. P. De Leon, Nanoscale diamond quantum sensors for many-body physics, *Nature Reviews Physics* **6**, 753 (2024).
- [6] E. Bauch, S. Singh, J. Lee, C. A. Hart, J. M. Schloss, M. J. Turner, J. F. Barry, L. M. Pham, N. Bar-Gill, S. F. Yelin, and R. L. Walsworth, Decoherence of ensembles of nitrogen-vacancy centers in diamond, *Physical Review B* **102**, 134210 (2020).
- [7] H. Park, J. Lee, S. Han, S. Oh, and H. Seo, Decoherence of nitrogen-vacancy spin ensembles in a nitrogen electron-nuclear spin bath in diamond, *npj Quantum Information* **8**, 95 (2022).
- [8] C. E. Bradley, J. Randall, M. H. Abobeih, R. C. Berrevoets, M. J. Degen, M. A. Bakker, M. Markham,

[21] M. W. Doherty, N. B. Manson, P. Delaney, F. Jelezko, J. Wrachtrup, and L. C. Hollenberg, The nitrogen-vacancy colour centre in diamond, *Physics Reports* **528**, 1 (2013).

[22] R. Hanson, F. M. Mendoza, R. J. Epstein, and D. D. Awschalom, Polarization and Readout of Coupled Single Spins in Diamond, *Physical Review Letters* **97**, 087601 (2006).

[23] M. Loretz, H. Takahashi, T. F. Segawa, J. M. Boss, and C. L. Degen, Optical hyperpolarization of nitrogen donor spins in bulk diamond, *Physical Review B* **95**, 064413 (2017).

[24] S. R. Hartmann and E. L. Hahn, Nuclear Double Resonance in the Rotating Frame, *Physical Review* **128**, 2042 (1962).

[25] C. Belthangady, N. Bar-Gill, L. M. Pham, K. Arai, D. Le Sage, P. Cappellaro, and R. L. Walsworth, Dressed-State Resonant Coupling between Bright and Dark Spins in Diamond, *Physical Review Letters* **110**, 157601 (2013).

[26] A. Laraoui and C. A. Meriles, Approach to Dark Spin Cooling in a Diamond Nanocrystal, *ACS Nano* **7**, 3403 (2013).

[27] G. Kucsko, S. Choi, J. Choi, P. C. Maurer, H. Zhou, R. Landig, H. Sumiya, S. Onoda, J. Isoya, F. Jelezko, E. Demler, N. Y. Yao, and M. D. Lukin, Critical Thermalization of a Disordered Dipolar Spin System in Diamond, *Physical Review Letters* **121**, 023601 (2018).

[28] J. Lee, M. Tatsuta, A. Xu, E. Bauch, M. J. H. Ku, and R. L. Walsworth, Dressed-state control of effective dipolar interaction between strongly-coupled solid-state spins, *npj Quantum Information* **9**, 77 (2023).

[29] H. S. Knowles, D. M. Kara, and M. Atatüre, Demonstration of a Coherent Electronic Spin Cluster in Diamond, *Physical Review Letters* **117**, 100802 (2016).

[30] V. Ranjan, G. De Lange, R. Schutjens, T. Debelhoir, J. P. Groen, D. Szombati, D. J. Thoen, T. M. Klapwijk, R. Hanson, and L. DiCarlo, Probing Dynamics of an Electron-Spin Ensemble via a Superconducting Resonator, *Physical Review Letters* **110**, 067004 (2013).

[31] N. A. Prisco, A. C. Pinon, L. Emsley, and B. F. Chmelka, Scaling analyses for hyperpolarization transfer across a spin-diffusion barrier and into bulk solid media, *Physical Chemistry Chemical Physics* **23**, 1006 (2021).

[32] See Supplemental Material for experimental details, theoretical derivations, and numerical simulation methods.

[33] G. De Lange, T. Van Der Sar, M. Blok, Z.-H. Wang, V. Dobrovitski, and R. Hanson, Controlling the quantum dynamics of a mesoscopic spin bath in diamond, *Scientific Reports* **2**, 382 (2012).

[34] K. Rezai, S. Choi, M. D. Lukin, and A. O. Sushkov, Probing Dynamics of a Two-Dimensional Dipolar Spin Ensemble Using Single Qubit Sensor, *Physical Review Letters* **134**, 050801 (2025).

[35] L. Robledo, H. Bernien, T. van der Sar, and R. Hanson, Spin dynamics in the optical cycle of single nitrogen-vacancy centres in diamond, *New Journal of Physics* **13**, 025013 (2011).

[36] J. C. Marcks, M. Onizhuk, Y.-X. Wang, Y. Zhu, Y. Jin, B. S. Soloway, M. Fukami, N. Delegan, F. J. Heremans, A. A. Clerk, G. Galli, and D. D. Awschalom, Quantum Spin Probe of Single Charge Dynamics, *Physical Review Letters* **133**, 130802 (2024).

[37] G. Wang, C. Li, H. Tang, B. Li, F. Madonini, F. F. Alsallom, W. K. Calvin Sun, P. Peng, F. Villa, J. Li, and P. Cappellaro, Manipulating solid-state spin concentration through charge transport, *Proceedings of the National Academy of Sciences* **120**, e2305621120 (2023).

[38] J. Choi, S. Choi, G. Kucsko, P. C. Maurer, B. J. Shields, H. Sumiya, S. Onoda, J. Isoya, E. Demler, F. Jelezko, N. Y. Yao, and M. D. Lukin, Depolarization Dynamics in a Strongly Interacting Solid-State Spin Ensemble, *Physical Review Letters* **118**, 093601 (2017).

[39] I. Schwartz, J. Scheuer, B. Tratzmiller, S. Müller, Q. Chen, I. Dhand, Z.-Y. Wang, C. Müller, B. Naydenov, F. Jelezko, and M. B. Plenio, Robust optical polarization of nuclear spin baths using Hamiltonian engineering of nitrogen-vacancy center quantum dynamics, *Science Advances* **4**, eaat8978 (2018).

[40] J. Choi, H. Zhou, H. S. Knowles, R. Landig, S. Choi, and M. D. Lukin, Robust Dynamic Hamiltonian Engineering of Many-Body Spin Systems, *Physical Review X* **10**, 031002 (2020).

[41] J. Baugh, O. Moussa, C. A. Ryan, A. Nayak, and R. Laflamme, Experimental implementation of heat-bath algorithmic cooling using solid-state nuclear magnetic resonance, *Nature* **438**, 470 (2005).

[42] S. Zaiser, C. T. Cheung, S. Yang, D. B. R. Dasari, S. Raeisi, and J. Wrachtrup, Cyclic cooling of quantum systems at the saturation limit, *npj Quantum Information* **7**, 92 (2021).

[43] G. Goldstein, P. Cappellaro, J. R. Maze, J. S. Hodges, L. Jiang, A. S. Sørensen, and M. D. Lukin, Environment-Assisted Precision Measurement, *Physical Review Letters* **106**, 140502 (2011).

[44] R. Goldblatt, A. Martin, and A. Wood, Sensing Coherent Nuclear Spin Dynamics with an Ensemble of Paramagnetic Nitrogen Spins, *PRX Quantum* **5**, 020334 (2024).

[45] D. Pagliero, K. R. K. Rao, P. R. Zangara, S. Dhomkar, H. H. Wong, A. Abril, N. Aslam, A. Parker, J. King, C. E. Avalos, A. Ajoy, J. Wrachtrup, A. Pines, and C. A. Meriles, Multispin-assisted optical pumping of bulk C 13 nuclear spin polarization in diamond, *Physical Review B* **97**, 024422 (2018).

[46] T.-X. Zheng, A. Li, J. Rosen, S. Zhou, M. Koppenhöfer, Z. Ma, F. T. Chong, A. A. Clerk, L. Jiang, and P. C. Maurer, Preparation of metrological states in dipolar-interacting spin systems, *npj Quantum Information* **8**, 150 (2022).

[47] W. Wu, E. J. Davis, L. B. Hughes, B. Ye, Z. Wang, D. Kufel, T. Ono, S. A. Meynell, M. Block, C. Liu, H. Yang, A. C. Bleszynski Jayich, and N. Y. Yao, Spin squeezing in an ensemble of nitrogen-vacancy centres in diamond, *Nature* **646**, 74 (2025).

[48] S. Choi, J. Choi, R. Landig, G. Kucsko, H. Zhou, J. Isoya, F. Jelezko, S. Onoda, H. Sumiya, V. Khemani, C. von Keyserlingk, N. Y. Yao, E. Demler, and M. D. Lukin, Observation of discrete time-crystalline order in a disordered dipolar many-body system, *Nature* **543**, 221 (2017).

[49] C. M. Selco, C. Bengs, C. Shah, Z. Zhang, and A. Ajoy, Emergent Decoherence Dynamics in Doubly Disordered Spin Networks (2025), arXiv:2511.07785 [quant-ph].

# Supplemental Material for “Mesoscopic Spin Coherence in a Disordered Dark Electron Spin Ensemble”

Taewoong Yoon,<sup>1,2</sup> Sangwon Oh,<sup>3</sup> Junghyun Lee,<sup>4,\*</sup> and Hyunyong Choi<sup>1,2,†</sup>

<sup>1</sup>*Department of Physics and Astronomy, Seoul National University, Seoul 08826, Korea*

<sup>2</sup>*Institute of Applied Physics, Seoul National University, Seoul 08826, Korea*

<sup>3</sup>*Department of Physics and Department of Energy Systems Research, Ajou University, Suwon 16499, Korea*

<sup>4</sup>*Center for Quantum Technology, Korea Institute of Science and Technology, Seoul 02792, Korea*

(Dated: February 20, 2026)

## I. EXPERIMENTAL DETAILS

Experiments are performed at room temperature on a chemical vapor deposition (CVD) diamond substrate (Element Six) containing a 40  $\mu\text{m}$  thick, 99.9%  $^{12}\text{C}$ -enriched epitaxial layer. Isotopic purification suppresses  $^{13}\text{C}$  nuclear spin bath contributions, such that the electron spin dynamics are predominantly governed by dipolar interactions between NV centers and P1 centers.

Optical initialization and readout are conducted using a home-built confocal microscope. A 532 nm continuous-wave laser (CNI MLL-III-532-200mW) serves as the excitation source, with intensity and pulse timing controlled by an acousto-optic modulator (Crystal Technology 3200-147) in a double-pass configuration achieving an extinction ratio  $> 50$  dB. The laser power is set to 10  $\mu\text{W}$  for initial NV polarization and fluorescence readout, and elevated to 50  $\mu\text{W}$  during polarization transfer cycles for faster NV re-initialization. The beam is focused onto the sample via an oil-immersion objective (NA 1.42, Olympus PLAPON60XO). Photoluminescence is collected through the same objective, spectrally filtered (650–792 nm), and detected by a single-photon counting module (Excelitas SPCM-ARQH-14-FC).

Independent addressing of NV and P1 centers is achieved using two microwave sources. Vector signal generators (SRS SG396 and Anritsu MG3700A) provide carrier frequencies, modulated by an arbitrary waveform generator (Zurich Instruments HDAWG) to synthesize amplitude- and phase-modulated pulses. The signals are combined (Mini-Circuits ZN2PD2-63-S+), amplified by 45 dB (Mini-Circuits ZHL-16W-43-S+), and delivered to the diamond through a gold coplanar waveguide lithographically patterned on a glass coverslip.

A static magnetic field of 446 G is applied and aligned along the [111] crystal axis using three cylindrical samarium-cobalt magnets mounted on motorized linear stages (Zaber X-LRM-100A-DE51). All experimental sequences, laser modulation, and gated photon counting are synchronized by the HDAWG operating at 2.4 GS/s.

## II. EFFECTIVE HAMILTONIANS FOR THE NV-P1 SYSTEM

The magnetic dipole-dipole interaction between electron spins  $i$  and  $j$  separated by distance  $r_{ij}$  is

$$H_{\text{dip}}^{ij} = -\frac{J_0}{r_{ij}^3} [3(\mathbf{S}_i \cdot \hat{\mathbf{n}})(\mathbf{S}_j \cdot \hat{\mathbf{n}}) - \mathbf{S}_i \cdot \mathbf{S}_j], \quad (\text{S1})$$

where  $J_0 = \mu_0 \gamma_e^2 \hbar / (4\pi) \approx 52 \text{ MHz}\cdot\text{nm}^3$  is the dipolar coupling constant and  $\hat{\mathbf{n}} = \mathbf{r}_{ij}/r_{ij}$  is the unit inter-spin vector. We derive the effective Hamiltonians in two successive steps: the secular approximation in the rotating frame, followed by the dressed-state transformation under continuous driving.

### A. Dipolar Interactions in the Rotating Frame

Transforming to the rotating frame via  $U(t) = \exp(i \sum_k \omega_k S_k^z t)$ , the spin operators evolve as  $S^z \rightarrow S^z$  and  $S^\pm \rightarrow S^\pm e^{\pm i\omega t}$ , where  $S^\pm = S^x \pm iS^y$ . Expressing the dipolar Hamiltonian in terms of these ladder operators and applying the secular approximation yields different effective Hamiltonians depending on the frequency mismatch between the interacting spins.

\* jh\_lee@kist.re.kr

† hy.choi@snu.ac.kr

For spins sharing the same resonance frequency, such as NV centers along a common crystallographic axis or P1 centers, the degenerate Larmor frequencies ( $\omega_i = \omega_j$ ) render the flip-flop terms time-independent while the double-quantum terms oscillate at  $2\omega$  and average to zero:

$$H_{\text{intra}}^{ij} = -\frac{J_0}{r_{ij}^3} \left[ \frac{1 - 3 \cos^2 \theta_{ij}}{4} (S_i^+ S_j^- + S_i^- S_j^+) + (3 \cos^2 \theta_{ij} - 1) S_i^z S_j^z \right], \quad (\text{S2})$$

where  $\theta_{ij}$  is the angle between  $\mathbf{r}_{ij}$  and the quantization axis. Defining the effective dipolar coupling  $J_{ij} = J_0(1 - 3 \cos^2 \theta_{ij})/r_{ij}^3$ , the flip-flop terms mediate energy-conserving spin exchange with strength  $J_{ij}/4$ , while the Ising term  $S_i^z S_j^z$  produces configuration-dependent energy shifts.

For NV-P1 pairs, the large frequency mismatch  $|\omega_{\text{NV}} - \omega_{\text{P1}}| \sim 370$  MHz, arising from the NV zero-field splitting ( $\approx 2.87$  GHz) and the external magnetic field ( $B = 446$  G), suppresses the flip-flop terms, leaving a purely Ising interaction:

$$H_{\text{inter}}^{ij} = -\frac{J_0}{r_{ij}^3} (3 \cos^2 \theta_{ij} - 1) S_i^z S_j^z. \quad (\text{S3})$$

This causes the P1 bath to act as a fluctuating magnetic field for the NV ensemble, contributing to dephasing but precluding coherent polarization transfer.

## B. Effective Interactions in the Dressed Frame

In the double spin-locking protocol, continuous microwave drives are applied at the NV and P1 resonance frequencies, adding

$$H_{\text{drive}} = \Omega_{\text{NV}} S_{\text{NV}}^x + \Omega_{\text{P1}} S_{\text{P1}}^x \quad (\text{S4})$$

to the rotating-frame Hamiltonian, where  $\Omega_{\text{NV}}$  and  $\Omega_{\text{P1}}$  are the Rabi frequencies. When  $\Omega \gg |J_{ij}|$ , the drive defines a new quantization axis along  $x$ . We introduce tilted-frame ladder operators  $\tilde{S}^\pm = S^y \pm iS^z$ , with inverse relations  $S^y = (\tilde{S}^+ + \tilde{S}^-)/2$  and  $S^z = (\tilde{S}^+ - \tilde{S}^-)/(2i)$ . In the interaction picture of  $H_{\text{drive}}$ , the tilted-frame operators evolve as  $\tilde{S}_k^\pm(t) = \tilde{S}_k^\pm e^{\pm i\Omega_k t}$ . Rewriting the bilinear spin products in the tilted frame and dropping the double-quantum terms oscillating at  $\pm 2\Omega$ , the two transverse products yield identical secular parts:

$$S_i^y S_j^y, S_i^z S_j^z \longrightarrow \frac{1}{4} (\tilde{S}_i^+ \tilde{S}_j^- + \tilde{S}_i^- \tilde{S}_j^+), \quad (\text{S5})$$

while  $S_i^x S_j^x$  is time-independent and unchanged.

### 1. Intra-group interactions

Rewriting Eq. (S2) in Cartesian form using  $S_i^+ S_j^- + S_i^- S_j^+ = 2(S_i^x S_j^x + S_i^y S_j^y)$  and applying Eq. (S5) to the  $S^y S^y$  and  $S^z S^z$  terms yields:

$$\tilde{H}_{\text{intra}}^{ij} = \frac{J_{ij}}{8} (\tilde{S}_i^+ \tilde{S}_j^- + \tilde{S}_i^- \tilde{S}_j^+) - \frac{J_{ij}}{2} S_i^x S_j^x. \quad (\text{S6})$$

This retains the structure of Eq. (S2) but with the quantization axis rotated from  $z$  to  $x$  and the coupling rescaled by a factor of  $-1/2$ : the flip-flop strength becomes  $J_{ij}/8$  and the Ising term  $S_i^x S_j^x$  has coefficient  $-J_{ij}/2$ .

### 2. Inter-group NV-P1 interactions

For the Ising Hamiltonian Eq. (S3), applying Eq. (S5) converts  $S_i^z S_j^z$  into flip-flop terms with time dependence  $e^{\pm i(\Omega_{\text{NV}} - \Omega_{\text{P1}})t}$ . Under the Hartmann-Hahn condition  $\Omega_{\text{NV}} = \Omega_{\text{P1}} \equiv \Omega$ , these become time-independent:

$$\tilde{H}_{\text{inter}}^{ij} = \frac{J_{ij}}{4} (\tilde{S}_i^+ \tilde{S}_j^- + \tilde{S}_i^- \tilde{S}_j^+). \quad (\text{S7})$$

The Ising interaction that suppressed NV-P1 cross-relaxation is thus converted into coherent spin exchange with flip-flop coupling  $J_{ij}/4$ , identical in form to the lab-frame intra-group flip-flop interaction Eq. (S2). This coupling determines the transition rates in the spin diffusion model (Sec. V).

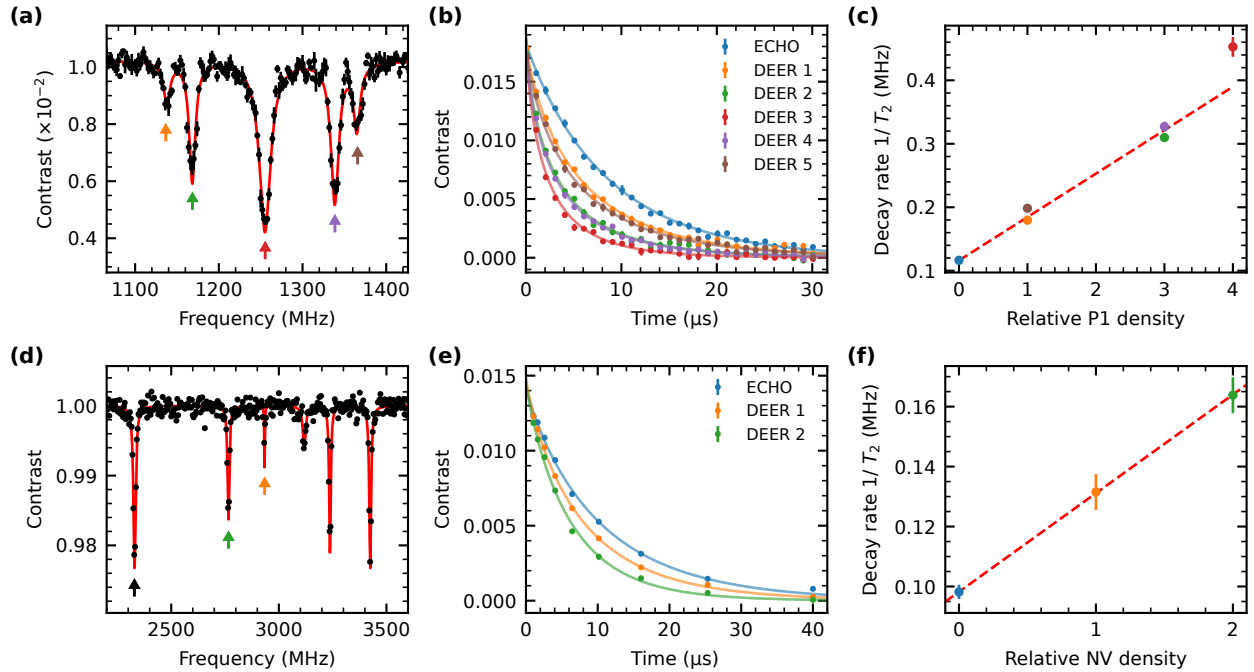


FIG. S1. Experimental characterization of P1 and NV spin baths. (a) DEER spectrum of P1 centers. Colored arrows indicate the addressed resonance frequencies corresponding to different hyperfine and Jahn-Teller subgroups. (b) DEER decay traces for each P1 subgroup. (c) Extracted dephasing rates ( $1/T_2$ ) versus relative P1 density. Point colors correspond to the resonance dips marked in (a). (d) CW-ODMR spectrum of NV centers under a magnetic field aligned along [1, 1, 1.5]. The black arrow indicates the sensor NV resonance, and colored arrows indicate the bath NV resonances. (e) DEER decay traces for each NV group configuration ( $\{1 : 0, 1 : 1, 1 : 2\}$ ). (f) Extracted dephasing rates versus relative NV density. Point colors correspond to the arrows in (d).

### III. ESTIMATION OF NV AND P1 CONCENTRATIONS

We estimate the absolute densities of NV and P1 centers by comparing experimental double electron-electron resonance (DEER) measurements with numerical quantum dynamics simulations based on the Hamiltonians derived in Sec. II. While it is well-established that the spin dephasing rate  $1/T_2$  scales linearly with the density of the surrounding magnetic spin bath, determining the absolute concentration remains challenging because the proportionality constant depends on the specific spin species, their spatial distribution, and the experimental pulse sequences [1].

#### A. Experimental DEER Measurements

The experimental DEER spectra and decay traces are summarized in Fig. S1. We measure the dephasing rates as a function of the relative spin density for each subgroup. The DEER sequence applies a  $\pi$  pulse on the bath spins during a Hahn-echo sequence on the sensor spin, allowing isolation of the dephasing contribution from the addressed bath spins.

For NV-P1 DEER, we address individual P1 hyperfine subgroups at the main experimental field of 446 G. The P1 spectrum consists of five resolvable dips arising from the  $^{14}\text{N}$  hyperfine interaction and Jahn-Teller distortion, with population fractions  $\{1, 3, 4, 3, 1\}/12$ . By sequentially addressing different subgroups, we measure the dephasing rate as a function of the relative P1 density.

For NV-NV DEER measurements, a magnetic field of approximately 200 G is aligned along the [1, 1, 1.5] crystallographic direction. This alignment ensures that two of the four NV axis groups are energetically degenerate, allowing us to tune the effective number of bath spins by addressing these overlapping resonances. We perform measurements for three distinct sensor-to-bath configurations:  $\{1 : 0, 1 : 1, 1 : 2\}$ , where the  $1 : 0$  case corresponds to a standard Hahn-echo (no bath spins flipped) and the  $1 : 1$  and  $1 : 2$  cases involve addressing one or two bath groups, respectively. By performing a linear fit to the decay rates extracted from these traces, we obtain the experimental slope  $\gamma_{\text{exp}}$  in units of MHz/group.

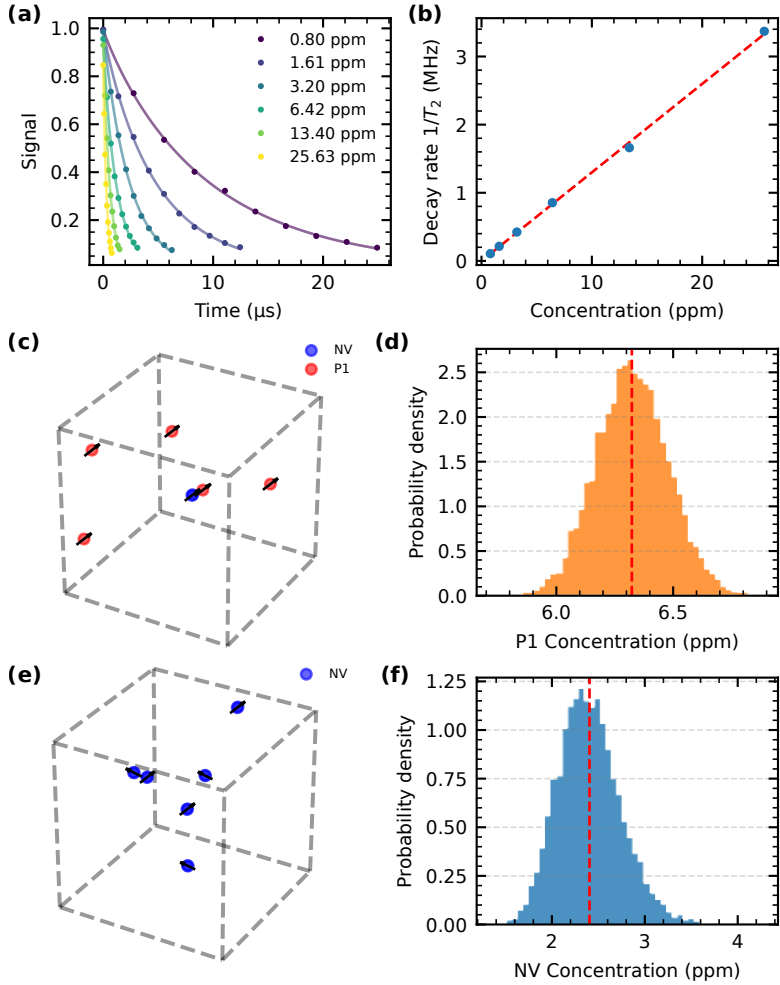


FIG. S2. Numerical simulation of DEER dynamics in disordered spin clusters. (a) Simulated NV-P1 DEER decay traces at various P1 concentrations (0.8–26 ppm). (b) Simulated dephasing rates as a function of absolute P1 density. The dashed line is a linear fit. (c) Representative NV-P1 cluster configuration used in the simulation. (d) Probability distribution of the estimated P1 concentration from Monte Carlo uncertainty propagation. (e) Representative NV cluster configuration used for NV-NV DEER simulations. (f) Probability distribution of the estimated NV concentration from Monte Carlo uncertainty propagation. All dynamical results are averaged over 1000 random realizations.

## B. Quantum Dynamics Simulation

To calibrate the experimental slopes and extract absolute concentrations, we perform numerical simulations [Fig. S2] using a disordered dipolar spin model implemented in the QuTiP framework [2]. Spin positions are generated on a diamond lattice (lattice constant  $a = 0.3567$  nm) within a cubic simulation volume. Each defect is assigned one of the four  $\langle 111 \rangle$  crystallographic orientations according to the specified axis distribution. Configurations with nearest-neighbor distances less than 1 nm are excluded.

For NV-P1 DEER, we model a cluster consisting of 1 NV sensor and 5 P1 bath spins treated quantum mechanically, while for NV-NV DEER, we consider a cluster of 6 NV centers distributed among the relevant axis groups (e.g.,  $\{2, 2, 2, 0\}$ ). The system Hamiltonian is constructed from Eqs. (S2) and (S3): spins sharing the same type and axis interact via the full secular Hamiltonian (flip-flop + Ising), while heterogeneous pairs (different species or axes) interact via the Ising term only. For NV centers, the effective spin-1/2 operators are scaled by  $\sqrt{2}$  to account for the  $|0\rangle \leftrightarrow |-1\rangle$  subspace transitions in spin 1 matrix elements.

The decay traces are fitted to a stretched exponential function  $S(t) = A \exp[-(t/T_2)^\beta]$ , from which the dephasing rate  $1/T_2$  is extracted. To capture ensemble-averaged behavior arising from intrinsic positional disorder, we average the dynamics over 1000 independent random spatial realizations for each density point. The concentration-dependent

simulation is performed at multiple target densities spanning 0.8–200 ppm, with the evolution time scaled inversely with concentration to ensure adequate sampling of the decay dynamics.

### C. Concentration Determination

The simulated dephasing rates are fitted to a linear model  $\Gamma = \alpha \cdot n$ , yielding the numerical dephasing coefficient  $\alpha$  [MHz/ppm] for each subgroup configuration. To account for the sensor-bath configurations used in the experiment, we calculate the simulated DEER slope  $K$  [MHz/(group·ppm)] by evaluating the expected dephasing rate for each group configuration at a total density of 1 ppm.

The total ensemble density is determined by the ratio  $n_{\text{total}} = \gamma_{\text{exp}}/K$ . To rigorously propagate the uncertainties from both the experimental fit and the numerical simulation, we employ a Monte Carlo analysis ( $N = 10,000$ ). In each iteration, values for the experimental slopes and numerical dephasing coefficients are sampled from their respective Gaussian distributions.

Following this estimation procedure, we determine the total NV density to be  $[\text{NV}] = 2.4 \pm 0.3$  ppm and the total P1 density to be  $[\text{P1}] = 6.3 \pm 0.2$  ppm. The corresponding concentration ratio is  $n_{\text{P1}}/n_{\text{NV}} \approx 2.6$ . These values are consistent with independent estimates obtained by applying established dephasing-rate calibrations [3–5] to the measured  $T_2^* = 1.58 \pm 0.01$   $\mu\text{s}$  and  $T_2 = 10.7 \pm 1.0$   $\mu\text{s}$  of our sample.

## IV. ESTIMATION OF P1 POLARIZATION

We derive the relationship between the measured signal contrast and the P1 bath polarization by considering angular momentum conservation during double spin-locking at the Hartmann-Hahn condition. Let  $n_{\text{NV}}$  and  $n_{\text{P1}}$  denote the spin densities of the addressed NV and P1 subgroups, respectively, and let  $P_{\text{NV},0}$  be the initial NV polarization after optical pumping. Upon reaching quasi-equilibrium under the HH condition, the total polarization in the rotating frame is conserved and redistributed between the two spin species.

For the parallel ( $\uparrow\uparrow$ ) configuration, where the P1 bath polarization is aligned with the NV polarization, the total initial polarization is  $P_{\text{tot}} = n_{\text{NV}}P_{\text{NV},0} + n_{\text{P1}}P_{\text{P1}}$ . After equilibration, this polarization is shared between the two species at a common polarization  $P_{\uparrow\uparrow}$ :

$$n_{\text{NV}}P_{\text{NV},0} + n_{\text{P1}}P_{\text{P1}} = (n_{\text{NV}} + n_{\text{P1}})P_{\uparrow\uparrow}. \quad (\text{S8})$$

For the antiparallel ( $\uparrow\downarrow$ ) configuration, the P1 polarization contributes with opposite sign:

$$n_{\text{NV}}P_{\text{NV},0} - n_{\text{P1}}P_{\text{P1}} = (n_{\text{NV}} + n_{\text{P1}})P_{\uparrow\downarrow}. \quad (\text{S9})$$

The measured spin-lock signal is normalized such that the NV polarization is linearly mapped to a contrast  $C$ . Assuming this linear response, the equilibrium polarizations can be written as  $P_{\uparrow\uparrow} = P_{\text{NV},0}C_{\uparrow\uparrow}$  and  $P_{\uparrow\downarrow} = P_{\text{NV},0}C_{\uparrow\downarrow}$ .

Subtracting Eq. (S9) from Eq. (S8):

$$2n_{\text{P1}}P_{\text{P1}} = (n_{\text{NV}} + n_{\text{P1}})P_{\text{NV},0}(C_{\uparrow\uparrow} - C_{\uparrow\downarrow}). \quad (\text{S10})$$

Solving for the P1 polarization:

$$P_{\text{P1}} = P_{\text{NV},0} \frac{\Delta C}{2} \left( 1 + \frac{n_{\text{NV}}}{n_{\text{P1}}} \right), \quad (\text{S11})$$

where  $\Delta C = C_{\uparrow\uparrow} - C_{\uparrow\downarrow}$  is the quasi-equilibrium amplitude measured in the experiment. This expression relates the observable differential contrast to the absolute P1 polarization through the density ratio  $n_{\text{NV}}/n_{\text{P1}}$ .

## V. NUMERICAL SIMULATION OF POLARIZATION DYNAMICS

### A. Rate Equation Model

Polarization transport in the spin-locked system is modeled by a semiclassical master equation derived from Fermi's Golden Rule [6, 7]. Both intra-group (Eq. (S6)) and inter-group (Eq. (S7)) flip-flop interactions contribute to the transition rates, with dressed-frame coupling strengths  $J_{ij}/8$  and  $J_{ij}/4$ , respectively.

In the presence of disorder, each spin  $i$  has a local detuning  $\delta_i$  from the drive frequency, so that the effective Rabi frequency becomes  $\Omega_{\text{eff},i} = \sqrt{\Omega^2 + \delta_i^2}$ . The tilt angle of the effective field away from the drive axis satisfies  $\sin \theta_i = \Omega/\Omega_{\text{eff},i}$ . Only the transverse component of  $S^z$  (perpendicular to the local effective field) participates in the dressed-frame flip-flop, reducing the coupling by a projection factor  $\sin \theta_i \sin \theta_j$ . The effective coupling entering the transition rate is therefore:

$$\tilde{J}_{ij} = \begin{cases} (J_{ij}/8) \sin \theta_i \sin \theta_j & (\text{intra-group}), \\ (J_{ij}/4) \sin \theta_i \sin \theta_j & (\text{inter-group}). \end{cases} \quad (\text{S12})$$

By Fermi's Golden Rule, the transition rate for a flip-flop process between spins  $i$  and  $j$  is given by the spectral overlap of the two spin lineshapes at the effective detuning  $\Delta_{ij}^{\text{eff}} = \Omega_{\text{eff},i} - \Omega_{\text{eff},j}$ :

$$R_{ij} = 2|\tilde{J}_{ij}|^2 \frac{\Gamma}{\Gamma^2 + (\Delta_{ij}^{\text{eff}})^2}, \quad (\text{S13})$$

where  $\Gamma = 0.15$  MHz is the half-width at half-maximum of the Hartmann-Hahn resonance [Fig. 1(d) of the main text].

In the continuum limit, polarization transport driven by flip-flop interactions is described by the spin diffusion equation:

$$\frac{\partial P(\mathbf{r}, t)}{\partial t} = D \nabla^2 P(\mathbf{r}, t) - \frac{P(\mathbf{r}, t)}{T_{1\rho}}, \quad (\text{S14})$$

where  $D$  is the spin diffusion coefficient and  $T_{1\rho}$  is the rotating-frame relaxation time. For a disordered discrete spin network, we solve the corresponding lattice master equation directly:

$$\frac{dP_i}{dt} = \sum_j R_{ij}(P_j - P_i) - \frac{P_i}{T_{1\rho,i}}, \quad (\text{S15})$$

where  $R_{ij}$  is the pairwise polarization transfer rate, the first term describes polarization exchange with all neighboring spins, and the second term accounts for intrinsic spin-lattice relaxation at each site.

## B. Network Model Implementation

To numerically simulate the polarization dynamics, we implement a discrete spin network model consisting of randomly distributed NV and P1 centers. Spins are placed at random positions, drawn uniformly, within a cubic simulation box of side length  $L$ . Configurations with nearest-neighbor distances less than 1 nm are excluded. The spin density is set to match the addressed P1 subgroup concentration of  $\sim 1.6$  ppm ( $= 6.3$  ppm  $\times 3/12$ ), corresponding to a mean inter-spin spacing of  $d_{\text{avg}} = n^{-1/3} \approx 15.3$  nm, where  $n = c_{\text{ppm}} \times 1.76 \times 10^{-4}$  nm $^{-3}$  is the number density.

For each pair of spins  $(i, j)$ , the dipolar coupling strength is computed as  $J_{ij} = J_0(1 - 3 \cos^2 \theta_{ij})/r_{ij}^3$ , where  $r_{ij}$  is the inter-spin distance and  $\theta_{ij}$  is the angle between the inter-spin vector and the external magnetic field. For NV centers, the coupling is scaled by  $\sqrt{2}$  to account for the NV  $S = 1$  spin projection.

Local disorder arises from variations in the effective magnetic field experienced by each spin due to the surrounding bath. We model this as a random detuning  $\delta_i$  drawn from a Gaussian distribution with standard deviation  $W = 1.36$  MHz, where  $W$  is the characteristic disorder scale extracted from the saturation amplitude measurements in the main text.

All reported results are averaged over 1000 independent random realizations of spin positions to account for positional disorder.

## C. Spin Diffusion Coefficient

The spin diffusion coefficient  $D$  is extracted from the mean-squared displacement (MSD) of the polarization distribution. Starting from a single polarized NV center at the origin, we track the spatial spreading of polarization into the surrounding P1 bath. The MSD is defined as:

$$\text{MSD}(t) = \frac{\sum_i P_i(t) r_i^2}{\sum_i P_i(t)}, \quad (\text{S16})$$

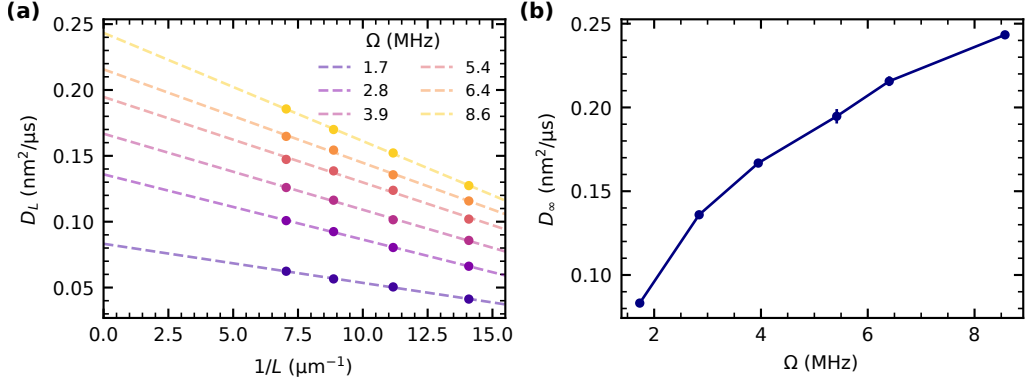


FIG. S3. Finite-size scaling of the spin diffusion coefficient. (a) Late-time diffusion coefficient  $D_L$  as a function of inverse system size  $1/L$  for various Rabi frequencies  $\Omega$ . For each  $\Omega$ ,  $D_L$  is extracted from the diffusive window ( $d_{\text{avg}}^2 < \text{MSD} < 0.5(L/2)^2$ ) via a linear fit. Dashed lines are linear extrapolations to the  $L \rightarrow \infty$  limit. (b) Extrapolated diffusion coefficient  $D_\infty$  versus Rabi frequency  $\Omega$ . Error bars represent the standard error of the linear regression intercept.

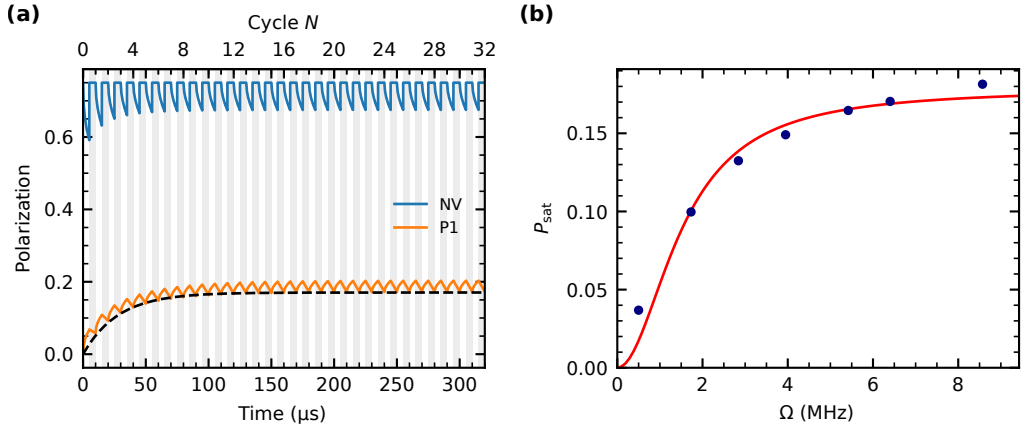


FIG. S4. Iterative polarization transfer simulation. (a) Simulated NV (blue) and P1 (orange) polarization dynamics under the iterative Hartmann-Hahn protocol at  $\Omega = 6.40$  MHz. The NV polarization is averaged over all NV centers and 1000 disorder realizations. The P1 polarization is averaged over the 8 nearest P1 centers to the NV source. The black dashed line is a saturation fit  $A(N) = P_{\text{sat}}(1 - e^{-N/N_{\text{sat}}})$ . Gray shading indicates the laser initialization phase. (b) Saturation polarization  $P_{\text{sat}}$  versus Rabi frequency  $\Omega$ . The red line is a fit to  $P_{\text{sat}}(\Omega) = P_\infty \Omega^2 / (\Omega^2 + \Omega_c^2)$ . Error bars represent  $1\sigma$  fitting uncertainties.

where  $r_i$  is the distance of spin  $i$  from the source NV. For normal diffusion in three dimensions,  $\text{MSD}(t) = 6Dt$ , allowing extraction of  $D$  from the linear regime of the MSD curve.

To obtain the  $L \rightarrow \infty$  limit of the diffusion coefficient (Fig. S3), we perform simulations at multiple system sizes ( $N_{\text{P1}} = 100, 200, 400, 800$  spins) and extract  $D$  from the late-time MSD slope within an analysis window bounded by the one-hop distance ( $\text{MSD}_{\text{start}} = d_{\text{avg}}^2$ ) and the finite-size effect onset ( $\text{MSD}_{\text{end}} = 0.5 \times (L/2)^2$ ). We extrapolate to the infinite-size limit using a linear fit of  $D$  versus  $1/L$ , where the intercept yields  $D_\infty$ .

At the experimental Rabi frequency  $\Omega = 6.40$  MHz, we obtain  $D \approx 0.22 \text{ nm}^2/\mu\text{s}$  in the  $L \rightarrow \infty$  limit. This value is used to estimate the spin diffusion length reported in the main text.

#### D. Iterative Polarization Transfer Simulation

To reproduce the experimentally observed saturation behavior, we incorporate a two-phase model that accounts for the different relaxation dynamics during the spin-lock (dark) and re-initialization (laser-on) phases of each polarization cycle.

Each polarization transfer cycle consists of two phases: (1) a 5  $\mu\text{s}$  interaction phase, during which NV and P1 spins interact under the Hartmann-Hahn condition with P1 relaxation governed by  $T_{1\rho}^{\text{P1}} = 430 \mu\text{s}$ , and (2) a 5  $\mu\text{s}$

NV initialization phase, during which NV spins are optically repolarized to  $P_{\text{NV},0} = 75\%$  while P1 spins experience enhanced relaxation with  $T_{1\rho,\text{laser}}^{\text{P1}} \approx 32 \mu\text{s}$ . The total cycle period is 10  $\mu\text{s}$ , and the simulation propagates the polarization state for up to 32 cycles.

The significantly shortened effective relaxation time during laser illumination is required to reproduce the observed saturation cycle number  $N_{\text{sat}} \approx 3$ . Such rapid depolarization is consistent with photo-ionization of P1 centers and associated charge-state dynamics within the local spin network under 532 nm illumination.

The two-phase simulation (Fig. S4) reproduces the Rabi-frequency dependence of the saturation amplitude  $A_{\text{sat}}(\Omega)$ , exhibiting the crossover behavior governed by the competition between driving strength and disorder.

While the model reproduces the qualitative saturation behavior, including  $N_{\text{sat}} \approx 3$  and the driving-strength dependence of  $A_{\text{sat}}(\Omega)$ , the simulated saturation polarization ( $P_{\infty} \approx 17.9\%$ ) overestimates the experimentally estimated value ( $P^{\text{P1}} \approx 7.4\%$ ) by a factor of 2–3. This discrepancy may originate from several sources: (i) the experimental polarization estimate assumes strict angular momentum conservation and complete quasi-equilibrium during the readout stage (Sec. IV), which may not hold if polarization leaks to unaddressed spin subgroups, (ii) the semiclassical model neglects quantum correlations among strongly coupled spins, which can reduce the effective transfer efficiency, and (iii) the use of a single phenomenological relaxation time  $T_{1\rho,\text{laser}}$  during laser illumination oversimplifies the position-dependent photo-ionization and charge-state dynamics.

---

[1] J. F. Barry, J. M. Schloss, E. Bauch, M. J. Turner, C. A. Hart, L. M. Pham, and R. L. Walsworth, Sensitivity optimization for NV-diamond magnetometry, *Reviews of Modern Physics* **92**, 015004 (2020).

[2] N. Lambert, E. Giguère, P. Menczel, B. Li, P. Hopf, G. Suárez, M. Gali, J. Lishman, R. Gadhvi, R. Agarwal, A. Galicia, N. Shammah, P. Nation, J. Johansson, S. Ahmed, S. Cross, A. Pitchford, and F. Nori, QuTiP 5: The Quantum Toolbox in Python, *Physics Reports* **1153**, 1 (2026).

[3] E. Bauch, S. Singh, J. Lee, C. A. Hart, J. M. Schloss, M. J. Turner, J. F. Barry, L. M. Pham, N. Bar-Gill, S. F. Yelin, and R. L. Walsworth, Decoherence of ensembles of nitrogen-vacancy centers in diamond, *Physical Review B* **102**, 134210 (2020).

[4] G. Wang, C. Li, H. Tang, B. Li, F. Madonini, F. F. Alsallom, W. K. Calvin Sun, P. Peng, F. Villa, J. Li, and P. Cappellaro, Manipulating solid-state spin concentration through charge transport, *Proceedings of the National Academy of Sciences* **120**, e2305621120 (2023).

[5] A. Chernyavskiy, I. Cojocaru, S. Drofa, P. Vilyuzhanina, A. Kozodaev, V. Vins, A. Smolyaninov, S.Ya. Kilin, S. Bolshedvorskii, V. Soshenko, and A. Akimov, Double electron resonance with two ensembles of nitrogen-vacancy centers in diamond, *Diamond and Related Materials* **160**, 113063 (2025).

[6] C. Zu, F. Machado, B. Ye, S. Choi, B. Kobrin, T. Mittiga, S. Hsieh, P. Bhattacharyya, M. Markham, D. Twitchen, A. Jarmola, D. Budker, C. R. Laumann, J. E. Moore, and N. Y. Yao, Emergent hydrodynamics in a strongly interacting dipolar spin ensemble, *Nature* **597**, 45 (2021).

[7] J. Choi, S. Choi, G. Kucsko, P. C. Maurer, B. J. Shields, H. Sumiya, S. Onoda, J. Isoya, E. Demler, F. Jelezko, N. Y. Yao, and M. D. Lukin, Depolarization Dynamics in a Strongly Interacting Solid-State Spin Ensemble, *Physical Review Letters* **118**, 093601 (2017).